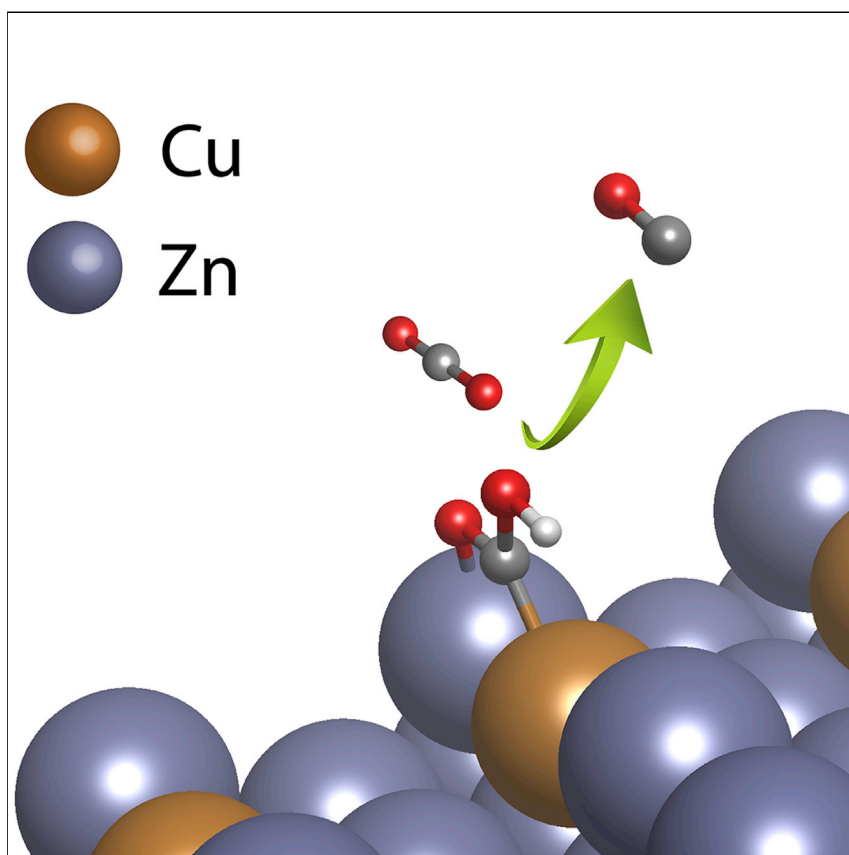


## Article

Bimetallic effects on Zn-Cu electrocatalysts enhance activity and selectivity for the conversion of CO<sub>2</sub> to CO

We achieve a >7-fold enhancement in intrinsic activity for electrochemical CO<sub>2</sub> reduction relative to a Zn-based electrode, by simply introducing a small quantity of Cu atoms onto the Zn surface. Detailed mechanistic investigations reveal that this improvement originates from a bimetallic effect between Zn and Cu, which can stabilize the key carboxyl intermediate during the CO<sub>2</sub> reduction to CO.

Lei Wang, Hongjie Peng, Sarah Lamaison, ..., Frank Abild-Pedersen, Thomas F. Jaramillo, Christopher Hahn

gregoire@caltech.edu (J.G.)  
abild@slac.stanford.edu (F.A.-P.)  
jaramillo@stanford.edu (T.F.J.)  
hahn31@lnl.gov (C.H.)

**Highlights**

A Zn-Cu electrocatalyst is prepared by a facile galvanic-exchange synthesis procedure

Zn-Cu electrodes demonstrate high selectivity (>95%) for CO<sub>2</sub> reduction to CO

Bimetallic effects stabilize the carboxyl intermediate during the CO<sub>2</sub> reduction



Wang et al., Chem Catalysis 1, 663–680  
August 19, 2021 © 2021 Elsevier Inc.  
<https://doi.org/10.1016/j.checat.2021.05.006>



## Article

Bimetallic effects on Zn-Cu electrocatalysts enhance activity and selectivity for the conversion of CO<sub>2</sub> to CO

Lei Wang,<sup>1,2,10</sup> Hongjie Peng,<sup>3,10</sup> Sarah Lamaison,<sup>1,4,10</sup> Zhifu Qi,<sup>1,5</sup> David M. Koshy,<sup>1</sup> Michaela Burke Stevens,<sup>1</sup> David Wakerley,<sup>1</sup> José A. Zamora Zeledón,<sup>1</sup> Laurie A. King,<sup>6</sup> Lan Zhou,<sup>7,8</sup> Yungchieh Lai,<sup>7</sup> Marc Fontecave,<sup>4</sup> John Gregoire,<sup>7,8,\*</sup> Frank Abild-Pedersen,<sup>3,\*</sup> Thomas F. Jaramillo,<sup>1,3,\*</sup> and Christopher Hahn<sup>3,9,11,\*</sup>

## SUMMARY

We report an active zinc-copper (Zn-Cu) bimetallic electrocatalyst for CO<sub>2</sub> reduction to CO, prepared by a facile galvanic procedure. Under moderate overpotentials, Zn-Cu catalysts that are Zn rich exhibit intrinsic activity for CO formation superior to that of pure Zn, Cu, and Ag, the last of which is the state-of-the-art catalyst in CO<sub>2</sub> electrolyzers. Combinatorial experiments involving catalysts prepared by physical vapor deposition reveal trends across the Zn-Cu system, corroborating the high CO selectivity unrivaled by other alloys and intermetallics. Physical and electrochemical characterization and first principles theory reveal that the origin of this synergy in intrinsic activity is an electronic effect from bimetallic Zn-Cu sites that stabilizes the carboxyl intermediate during CO<sub>2</sub> reduction to CO. Furthermore, by integrating Zn-Cu into gas-diffusion electrodes, we demonstrate that bimetallic effects lead to improved electrocatalytic performance at industrially relevant currents. These insights provide catalyst design principles that can guide future development of efficient and earth-abundant CO-producing electrocatalysts.

## INTRODUCTION

Syngas, a gas fuel mixture consisting primarily of CO and H<sub>2</sub>, is one of the most important resources in the chemical industry as a precursor for many products, including high-energy-density fuels, e.g., methanol, ammonia, and synthetic petroleum.<sup>1</sup> Active research on converting syngas to higher alcohols through either thermal or biocatalytic processes is expected to further boost the syngas industry.<sup>2,3</sup> As the majority of syngas is currently produced from fossil fuels,<sup>4</sup> it would be of great value to establish sustainable pathways to CO and H<sub>2</sub>. One such route for generating CO is electrochemical CO<sub>2</sub> reduction (CO<sub>2</sub>R), in which CO<sub>2</sub>, H<sub>2</sub>O, and renewable electricity can be used to upgrade CO<sub>2</sub> into CO. This is a promising strategy to mitigate CO<sub>2</sub> emissions by developing a carbon industry based on CO<sub>2</sub> that stores variable electricity from renewable sources in chemical form.<sup>5–7</sup>

Establishing catalyst design principles for maximizing selectivity and activity toward desired products is crucial for the industrialization of electrochemical CO<sub>2</sub>R. Many successful strategies have been reported for developing high-performance CO-production catalysts, including nanostructuring state-of-the-art Au and Ag catalysts,<sup>8–13</sup>

## The bigger picture

Electrochemical CO<sub>2</sub> reduction is a promising strategy for the sustainable synthesis of fuels and chemicals when combined with carbon-free electricity. A major challenge for the development of electrochemical CO<sub>2</sub> reduction has been establishing robust design principles that can guide the discovery of cost-effective catalysts, due to the complexity of the reaction networks. In this work, we discover a bimetallic effect between Zn and Cu that promotes synergistic performance for CO<sub>2</sub> reduction to CO superior to that of its pure component metals. The insights and catalyst structure-property relationships obtained can guide the future development of efficient and earth-abundant electrocatalysts for CO<sub>2</sub> reduction.



combining metals into multimetallic electrocatalysts,<sup>14–24</sup> incorporating first-row transition metals into heteroatom-doped graphitic carbons,<sup>25–31</sup> and immobilizing molecular catalysts onto electrode surfaces.<sup>32–35</sup> As shown in Figure 1, precious metal Au- and Ag-based materials remain the most active electrocatalysts for CO<sub>2</sub>R to CO, motivating the development of new catalysts comprising earth-abundant metals. In addition to their high intrinsic activity and selectivity for CO production, nanostructuring of Au and Ag materials has been shown to be a promising strategy to further improve their geometric activity by leveraging a combination of surface area effects,<sup>36</sup> local pH,<sup>11</sup> and field effects.<sup>9</sup> However, by normalizing the geometric activity of nanostructured Au and Ag electrodes to their corresponding electrochemically active surface areas (ECSAs), similar or even lower activity is obtained in comparison to that of planar Au and Ag foils, suggesting that increasing their electrode surface areas does not improve intrinsic activities. Transition metals and nitrogen-doped carbons (M-N-C) have also been extensively studied as CO-producing catalysts.<sup>25–31</sup> An important area of study is identifying and quantifying the active sites due to substantial heterogeneity of these materials with many distinct, isolated motifs. Efforts to understand these factors are critical to overcome the generally low density of active sites of M-N-C-type materials and to make them competitive with the precious metal catalysts on an electrode-area basis. Molecular catalysts are known to have high turnover frequency (TOF) per site for reducing CO<sub>2</sub> to CO, e.g., a TOF of  $\sim 10^4$  has been observed for an iron-porphyrin catalyst at an overpotential of 0.56 V.<sup>37</sup> After being immobilized to a conductive substrate, molecular catalysts behave similar to the M-N-Cs, which is expected due to the similarity of their active motifs.<sup>33–35</sup> Understanding how the intrinsic activity of the molecular catalyst is affected by heterogenization to the solid-electrolyte interface remains a significant research challenge.<sup>38</sup>

By mixing metals at the atomic level, e.g., through alloying, solid solutions, and intermetallic and segregated phases, the electronic properties of the resulting metallic surfaces can be modified and tuned to facilitate CO formation. Thus, bimetallic materials based on non-precious metals are promising for replacing the state-of-the-art Au- and/or Ag-based catalysts. In fact, several studies have demonstrated synergistic bimetallic effects for CO formation, showing enhanced activity with respect to the sum of their monometallic catalysts.<sup>14,24</sup> However, clear demonstrations of improving the intrinsic activity of CO<sub>2</sub>R to CO through bimetallic effects among non-precious metal catalysts are rare. Thus, further probing and understanding the mechanisms of bimetallic catalysts are needed to establish structure-performance relations, which can ultimately lead to improved intrinsic activity that is comparable to or higher than that of precious Au- and/or Ag-based catalysts. As Zn is the only non-precious material in the group of CO-producing monometals, it is a promising candidate for bimetallic studies.<sup>39</sup> However, Zn has a lower intrinsic activity and selectivity for CO<sub>2</sub>R to CO compared with Au and Ag (Figure 1),<sup>39–41</sup> which is likely related to the weak CO-binding energy on Zn surfaces.<sup>40,42</sup> As Cu has a moderate CO-binding energy, which is higher than that of Zn, incorporating Cu into Zn could, in principle, increase the CO-binding energy of the bimetallic surface and potentially upgrade its CO<sub>2</sub>R performance.<sup>40</sup> Previous efforts have shown that bimetallic alloys of Zn<sub>x</sub>Cu<sub>1-x</sub> (Zn-Cu) that are Zn rich are selective toward syngas (CO and H<sub>2</sub>),<sup>22</sup> while those that are Cu rich favor >2e<sup>-</sup> products.<sup>43–46</sup> These promising results motivate further studies to understand whether alloying Zn and Cu enhances the bimetallic intrinsic activity for CO<sub>2</sub>R to CO and the specific atomic-scale interactions between Zn and Cu (e.g., ligand and strain effects) that engender improved catalytic performance.

<sup>1</sup>SUNCAT Center for Interface Science and Catalysis, Department of Chemical Engineering, Stanford University, Stanford, CA 94305, USA

<sup>2</sup>Department of Chemical and Biomolecular Engineering, National University of Singapore, Singapore 117585, Singapore

<sup>3</sup>SUNCAT Center for Interface Science and Catalysis, SLAC National Accelerator Laboratory, Menlo Park, CA 94025, USA

<sup>4</sup>Sorbonne Universités, Collège de France, Laboratoire de Chimie des Processus Biologiques, CNRS UMR 8229, 75231 Paris, France

<sup>5</sup>Zhejiang Energy Technology Research Institute Co. Ltd., Hangzhou, Zhejiang 311121, China

<sup>6</sup>Faculty of Science and Engineering, Manchester Metropolitan University, Manchester M1 5GD, UK

<sup>7</sup>Joint Center for Artificial Photosynthesis, California Institute of Technology, Pasadena, CA 91125, USA

<sup>8</sup>Division of Engineering and Applied Science, California Institute of Technology, Pasadena, CA 91125, USA

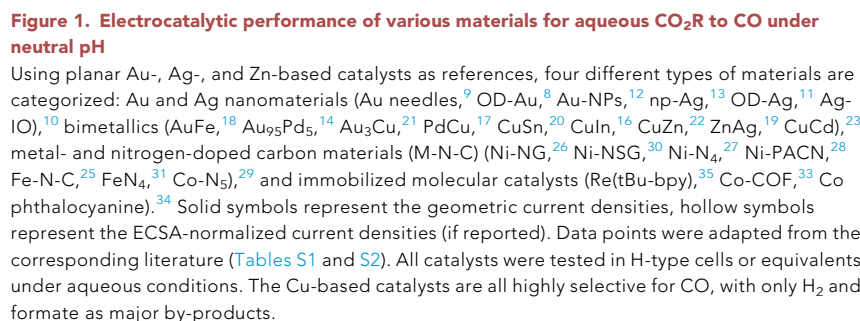
<sup>9</sup>Materials Science Division, Lawrence Livermore National Laboratory, Livermore, CA 94550, USA

<sup>10</sup>These authors contributed equally

<sup>11</sup>Lead contact

\*Correspondence: [gregoire@caltech.edu](mailto:gregoire@caltech.edu) (J.G.), [abild@slac.stanford.edu](mailto:abild@slac.stanford.edu) (F.A.-P.), [jaramillo@stanford.edu](mailto:jaramillo@stanford.edu) (T.F.J.), [hahn31@llnl.gov](mailto:hahn31@llnl.gov) (C.H.)

<https://doi.org/10.1016/j.checat.2021.05.006>



The Zn-Cu electrodes were prepared by immersing pre-polished polycrystalline Zn foils into a dilute  $\text{CuSO}_4$  solution at room temperature for a short period of time (referred to as “Zn-Cu (n s) electrodes,” where n s denotes time as 1, 5, 30,

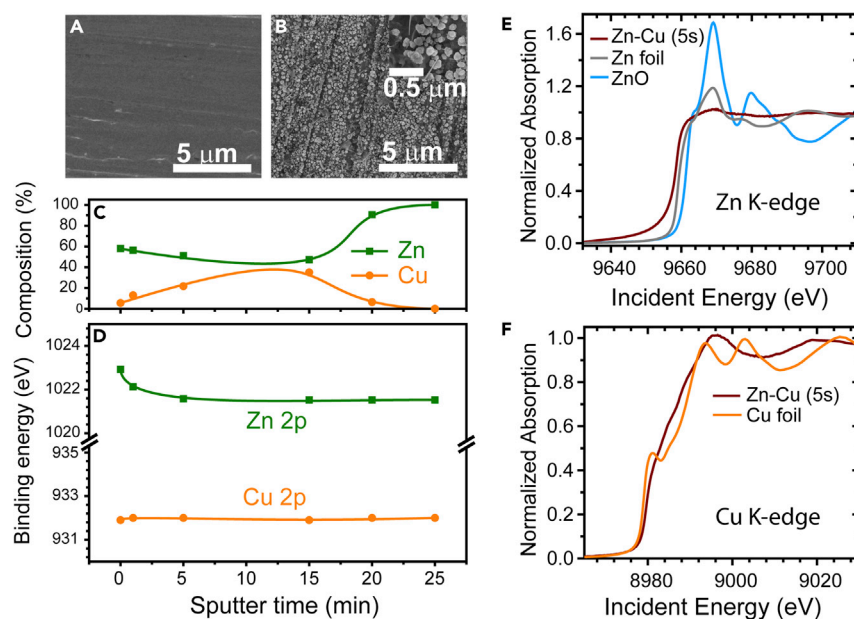


**Figure 2. Physical characterization of the Zn-Cu bimetallic surface**

(A and B) SEM of Zn foil before (A) and after (B) galvanic exchange for 5 s in 10 mM  $\text{CuSO}_4$ .

(C) XPS sputter-depth profiling of the Zn-Cu (5 s): the surface compositions of Zn and Cu as a function of sputtering time, the balance of the elements is oxygen.

(D) The  $2p_{3/2}$  peak positions of Zn and Cu at different sputtering times. The sputtering rate was ca. 1 nm/min.

(E and F) Normalized Zn K-edge (E) and Cu K-edge (F) X-ray absorption spectra for Zn-Cu (5 s); Zn foil, ZnO, and Cu foil are provided as references.

and 60 s). There is an obvious visual change upon deposition as the sample changes color from silver to black. A representative scanning electron microscopy (SEM) image of the Zn foil before and after 5 s of galvanic exchange is shown in Figures 2A and 2B, respectively. Notably, a layer of nanoparticles (50–100 nm in size) is seen to form on the surface of the Zn foil from this rapid treatment (Figure 2B), indicating that the galvanic-exchange procedure rapidly roughens the surface of Zn during the process. X-ray photoelectron spectroscopy (XPS) analysis suggests that the surfaces of these nanoparticles are enriched in Zn with a Zn:Cu ratio of  $\sim 10:1$  (Figure S1). A comparison of SEM and XPS data for 1, 5, 30, and 60 s Zn-Cu electrodes indicates that Cu composition and nanoparticle size increase concomitant with the reaction time (Figure S2). We propose that the surface roughening is a result of rapid Zn crystal deformation, starting from the grain boundaries and defects, likely due in part to the large thermodynamic driving force of the galvanic reaction ( $E_{\text{Cu}^{2+}/\text{Zn}}^0 = 1.1 \text{ V}$ ).<sup>47,48</sup> Grazing incidence X-ray diffraction (XRD) was performed (Figure S3) to assess the crystallinity of the prepared samples. No new XRD patterns emerged nor were expected for Zn-Cu bimetallic formation, due to a combination of the rough electrode surface, which will introduce a significant amount of bulk Zn signals even for grazing incidence configuration, and the similarity of the XRD patterns for Zn and Zn-Cu alloys that are Zn rich.<sup>44</sup> The absence of a pure Cu-metal phase, however, indicates a bimetallic surface without major phase separation. Atomic force microscopy (Figure S4) was introduced to directly measure the surface area differences between the Zn-Cu electrodes and the planar Zn-foil-based electrode. In addition, double-layer capacitance measurements (Figure S5) were also introduced to measure the increase in double-layer capacitance of Zn-Cu compared with that of Zn foil, since it should scale with the electrochemical active surface area. Increases of 1.35 and 2.5 times in surface

area were obtained for the Zn-Cu electrode by the above two different measurements, respectively. Thus, while the galvanic-exchange procedure nanostructures the surface, we conclude that it leads to relatively minor changes in the porosity of the electrodes.

### Electronic interactions between Zn and Cu in the near-surface region of Zn-Cu bimetallics

The Zn-Cu (5 s) electrode was probed with XPS to investigate its surface composition and electronic structure. The presence of XPS peaks at binding energies of 1,022.5 (Zn 2p<sub>3/2</sub>) and 1,045.5 eV (Zn 2p<sub>1/2</sub>) indicates that ZnO is present in the as-prepared sample. As Zn metal is readily oxidized by air to form a native oxide layer ( $\Delta_r G^\circ_{\text{ZnO}} = 320.5 \text{ kJ mol}^{-1}$ ),<sup>49</sup> we suggest that ZnO forms from oxygen exposure prior to the *ex situ* XPS measurement. This oxidation process is more rapid when the surface consists of nanoparticles,<sup>50</sup> which are present on the Zn-Cu samples in our work. Based on Pourbaix analysis of Zn,<sup>49</sup> we suggest that the native oxide is reduced to Zn metal under CO<sub>2</sub>R conditions. This hypothesis is in agreement with recent *ex situ* and *operando* characterization studies<sup>51,52</sup> that indicate metallic Zn is the active phase for electrochemical CO<sub>2</sub>R. On the other hand, Cu is likely in its metallic state in a Zn-Cu alloy (*vide infra*), as only a Cu 2p<sub>3/2</sub> peak was observed at a downshifted binding energy of 932.0 eV, with a notable absence of satellite peaks for both CuO and Cu<sub>2</sub>O, and ~1 eV lower than that of pure Cu metal.<sup>53</sup> This suggests a strong ligand effect from neighboring Zn atoms; later we describe our efforts involving XAS to further probe electronic structure. XPS depth profiling using argon sputtering shows that both the Zn:Cu ratio and the Zn 2p<sub>3/2</sub> peak position are dependent on the sputter time (Figures 2C, 2D, and S6). We hypothesize that the trend of Zn surface segregation arises because Zn is more oxophilic than Cu, which is commensurate with the aforementioned conclusion that ZnO is present on the surface. Conversely, the Cu 2p<sub>3/2</sub> peak position is consistent at ~932.0 eV, suggesting that the electronic structure of Cu is similar throughout the probe depth.

To further investigate these electronic interactions, we performed synchrotron XAS on the Zn and Cu K-edge within both their near-edge structure (XANES, Figures 2E and 2D) and their extended X-ray absorption fine structure (EXAFS) regions (Figure S7) for the Zn-Cu (5 s) electrode. Zn K-edge XANES revealed no prominent pre-edge feature for Zn-Cu (5 s), with a lower edge energy of 9,658.7 eV compared with 9,659 eV for the Zn-foil reference, suggesting that Zn within the Zn-Cu (5 s) electrode is mainly in a reduced state. Although XPS results indicate that ZnO is present on the surface of Zn-Cu (5 s), ZnO features were not observed in the XANES data for Zn-Cu (5 s); we attribute the lack of ZnO features in the XANES data to the large XAS probe depth (~1  $\mu\text{m}$ ) relative to the thin ZnO layer (<5–10 nm). Analysis of the Zn K-edge EXAFS region corroborates this conclusion, as there is a single scattering peak at 2.25 Å that is consistent with Zn-Zn metal bonding (Figure S7). Notably, the Cu K-edge XANES of Zn-Cu (5 s) shows substantially different features relative to those of the Cu-foil reference. In particular, the pre-edge peak at ~8,981 eV that is prominent for the Cu foil is greatly suppressed for Zn-Cu (5 s). Based on the calculated projected density of states for Zn 4s and Cu 4s orbitals in Zn-Cu (5 s) (Figure S8), we attribute this phenomenon to Zn donating 4s electron density to neighboring Cu atoms, which is in agreement with conclusions from previous studies on Zn-Cu alloys.<sup>54</sup> Similar to the XPS results, the Cu K-edge EXAFS data show a single peak at 2.25 Å, indicating that Cu is in a primarily metallic state (Figure S7). All the above evidence demonstrates that the galvanic-exchange process generates a well-mixed bimetallic system instead of a Cu layer on top of the bulk Zn metal. Moreover, there are strong electronic interactions between Zn and Cu atoms in the Zn-Cu (5 s)



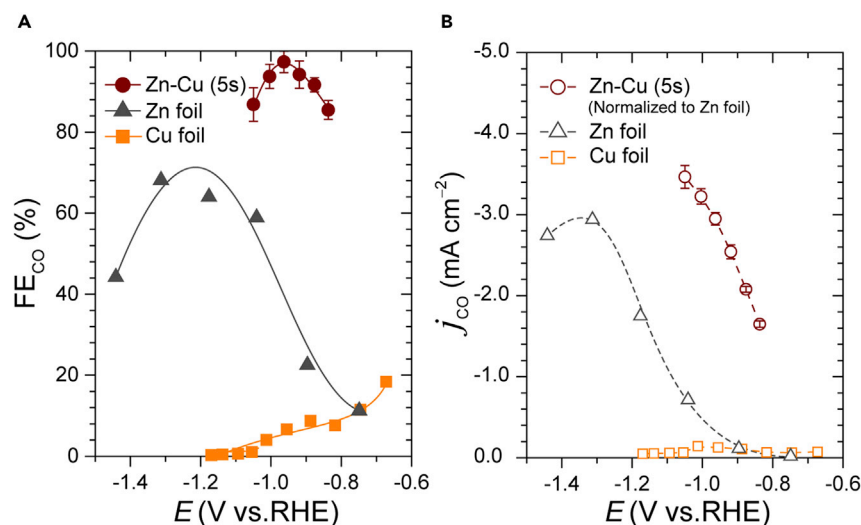


**Figure 3.** CO<sub>2</sub>R by Zn-Cu (5 s) bimetallic catalyst and its performance comparison to pristine Zn and Cu

Faradaic efficiencies (FE) and normalized partial current densities for CO formation on the Zn-Cu (5 s) bimetallic electrode and literature data for Zn and Cu electrodes,<sup>40</sup> as a function of the applied potential. Data points for Zn-Cu (5 s) are averaged from three individual measurements, the error bars represent the standard deviations (see Table S3). The only other measured products are H<sub>2</sub> and formate (Table S3).

bimetallic system, exhibiting distinct electronic properties in comparison to those of pure Zn and Cu.

### Electrocatalytic performance of Zn-Cu bimetallic electrodes

The electrocatalytic CO<sub>2</sub>R performance of the Zn-Cu electrodes was evaluated using 0.1 M KHCO<sub>3</sub> as the electrolyte in a two-compartment electrochemical cell. We first investigated how the surface concentration of Cu in Zn-Cu affects the CO<sub>2</sub>R activity by using a combination of cyclic voltammetry (CV) and chronoamperometry (CA) measurements to evaluate the 1, 5, 30, and 60 s Zn-Cu electrodes. The results indicate that the CO<sub>2</sub>R to CO activities do not scale linear with the surface Cu concentration and instead plateau after 5 s of the galvanic-exchange treatment (Figure S9). Thus, for the remainder of this work, we used the Zn-Cu (5 s) electrode as a platform for a deeper investigation of CO<sub>2</sub>R activity and selectivity.

To determine whether incorporating Cu into Zn enhances the intrinsic catalytic activity, we compared the electrocatalytic performance of Zn-Cu (5 s) with that of pure Zn and Cu. Initial CV measurements suggest that the Zn-Cu (5 s) electrode has a higher current density compared with pristine Zn and Cu electrodes under the same CO<sub>2</sub>R catalytic conditions (Figure S10), motivating more detailed CA measurements with product quantifications to confirm that the increase in current density is a result of enhancement in CO<sub>2</sub>R activity. As the galvanic-exchange procedure induces nanostructuring of Zn-Cu (5 s), we accounted for differences in the surface area of the electrodes by normalizing partial current densities to several metal-foil-based electrodes (Zn, Ag, Au) and employing several different surface area measurements (Figures S4, S5, and Note S1). At the same electrode potential (−0.96 V versus reversible hydrogen electrode [RHE]), Zn-Cu (5 s) is almost fully selective (97% Faradaic efficiency [FE]) for the CO pathway, whereas Zn is only 30% selective (FE) (Figure 3A). Formate and hydrogen are minor products evolved from Zn-Cu; no additional products were detected (Table S3). The normalized data indicate that Zn-Cu (5 s) is seven

times more active than pure Zn for CO<sub>2</sub>R to CO at an electrode potential of  $-0.96$  V versus RHE (Figure 3B). The above results indicate that Zn-Cu (5 s) is more selective than Zn for CO<sub>2</sub>R to CO by both improving the intrinsic catalytic activity for the CO<sub>2</sub>R to CO pathway and suppressing the competing hydrogen evolution reaction (HER). To compare the intrinsic catalytic activities of Zn-Cu (5 s) and Cu, we analyzed the normalized total CO<sub>2</sub> consumption rates to account for the fact that Cu is more selective for further reduced products beyond CO (Figure S11). This assessment clearly demonstrates that Zn-Cu (5 s) has a faster CO<sub>2</sub>R rate than pure Cu and Zn regardless of which product is being formed from CO<sub>2</sub>, indicating that incorporating Cu into Zn engenders a synergistic effect that improves the intrinsic CO<sub>2</sub>R activity of Zn-Cu bimetal beyond that of either of its component metals.

Since previous research has shown that nanostructuring CO<sub>2</sub>R electrocatalysts can also induce changes in selectivity through porosity effects,<sup>55</sup> we further investigated trends in reactivity using sputtered thin films of Zn-Cu with negligible surface roughness, since the thin-film-based electrodes are a reasonable approximation to the galvanic-exchange system due to their similar surface Zn:Cu ratio. A comparison of sputtered Zn<sub>10</sub>Cu<sub>1</sub> and Zn films across a range of electrode potentials shows similar trends in activity and selectivity compared with those described above for the Zn-Cu (5 s) and Zn foils (Figure S12). For example, the Zn<sub>10</sub>Cu<sub>1</sub> film in comparison to the Zn film exhibits significantly improved intrinsic activity and selectivity for CO<sub>2</sub>R to CO and suppressed intrinsic activity and selectivity for the HER. These results corroborate our conclusion that the aforementioned synergy in intrinsic activity is likely due to a bimetallic effect rather than an electrode surface-area effect. To better understand the impact of the electrode composition on reactivity, we also prepared and tested Zn<sub>1</sub>Cu<sub>10</sub> thin films to reflect the other extreme of a high Cu:Zn ratio for the sake of comparison. While these Zn<sub>1</sub>Cu<sub>10</sub> films show similar partial current densities for CO formation compared with Zn<sub>10</sub>Cu<sub>1</sub> films, the Zn<sub>1</sub>Cu<sub>10</sub> films are also more active and selective for the HER and for  $>2$  e<sup>-</sup> CO<sub>2</sub>R products, more similar to pure Cu. Thus, the results indicate that a Zn-rich surface is more favorable for applications that require high selectivity for CO<sub>2</sub>R to CO.

To assess a broader range of Zn-Cu bimetallic compositions, the study of sputtered films was extended to a composition library in which five compositions spanning 4%–70% Zn were synthesized. These films were examined for CO<sub>2</sub>R at  $-0.85$  V versus RHE using a specialized high-throughput electrochemical recirculation cell, enabling product distributions to be assessed after only 15 min of electrolysis. The results are shown in Figure S13 and demonstrate that the intrinsic activity and product selectivity vary dramatically with film composition. For lower concentrations of Zn, the HER activity increases substantially with increasing Zn concentration up to approximately 50%, reaching a current density of  $13.5 \text{ mA cm}^{-2}$  corresponding to an FE of over 83% for H<sub>2</sub>. Further increasing in Zn concentration from 50% to 70% results in more than 10-fold decrease in H<sub>2</sub> partial current density and more than 10-fold increase in CO partial current density. These trends continue with increasing Zn concentration to the Zn<sub>10</sub>Cu<sub>1</sub> catalyst noted above, which exhibits catalyst selectivity beyond that observed in any of the other alloy compositions. This maximum in CO selectivity coincides with the formation of a hexagonal close-packed (*hcp*) alloy in the sputter-deposited films, as was observed with the galvanic-exchange catalysts discussed above. The collective results involving Zn-Cu catalysts, prepared in various ways across a range of compositions and investigated in multiple laboratories, robustly demonstrate the unique catalytic properties of Cu alloyed in *hcp* Zn. This motivates theoretical investigations of the selectivity-enhancing mechanisms involved.



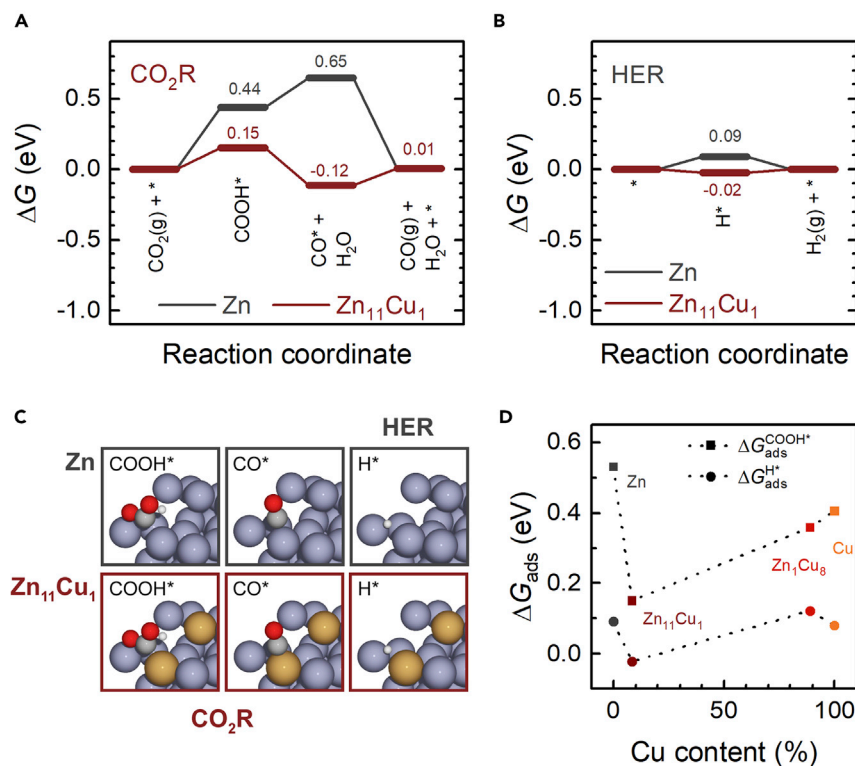


**Figure 4. DFT calculations**

(A and B) Free energy diagrams of CO<sub>2</sub>R to CO (1  $\mu$ bar) (A) and HER (B) on clean stepped *hcp* Zn(100) and *hcp* Zn<sub>11</sub>Cu<sub>1</sub>(100) surfaces at 0 V versus RHE. Each reduction step is assumed to proceed by transferring a proton-electron pair to the surface species. The potential of 0 V versus RHE is set to clearly show the PDS rather than reflecting the actual CO<sub>2</sub>R condition.

(C) Optimized atomistic configurations showing the adsorption of key intermediates (COOH\* and CO\* for CO<sub>2</sub>R; H\* for HER) on the surfaces. Purple gray, dark yellow, gray, red, and white spheres represent Zn, Cu, C, O, and H atoms, respectively.

(D) Adsorption free energies ( $\Delta G_{\text{ads}}$ ) of COOH\* and H\* on step sites as a function of the compositional fraction of Cu in the near-surface (top two) layers of different catalytic surfaces, where Zn<sub>1</sub>Cu<sub>8</sub> and Cu are in the fcc crystal structure.

### Theoretical insights on the impact of bimetallic effects on surface reactivity

The above experimental (Figure 2) and computational (Figure S6) results on Zn-Cu alloys suggest that the observed synergy in activity is related to an electronic effect between Zn and neighboring Cu atoms that affects the adsorption of key reaction intermediates. To gain further insight into this enhancement in performance, we carried out theoretical simulations based on DFT. Since undercoordinated sites have been identified as the major active sites for CO<sub>2</sub>R to CO,<sup>56</sup> we evaluated reaction energetics for both CO<sub>2</sub>R and the competing reaction HER, on stepped surfaces of Zn-Cu alloys with different surface compositions (see details under “computational details” and Figure S14). The CO<sub>2</sub>R mechanism is considered to proceed through the sequential two-step reduction of an adsorbed CO<sub>2</sub> to COOH\* and then to CO\* and water, followed by the desorption of CO (Figure 4A), while a Volmer-Heyrovsky mechanism is considered for HER (Figure 4B). Figure 4A shows that the potential-determining step (PDS) is the first protonation step to form COOH\*. The Zn<sub>11</sub>Cu<sub>1</sub> surface possesses a stronger COOH\* adsorption energy ( $\Delta G_{\text{ads}}^{\text{COOH}^*}$ ) by 0.15 eV compared with pristine Zn (0.44 eV), which can explain the earlier onset potential for CO production on the Zn-Cu (5 s) electrode. At sufficiently negative potentials (e.g., -0.96 V versus RHE), both CO formation and HER become

thermodynamically favorable (Figure S15). The suppression of the HER in Zn-Cu (5 s) is also explained by the computational modeling. On one hand, surface H\* is stabilized by incorporating Cu into Zn, which should in principle improve HER activity; however, this is not the case for two reasons. First, this effect is not as profound as that for COOH\*, indicating a smaller effect on the HER than on the CO<sub>2</sub>R (Figure 4B). Second, CO poisoning can have a substantial impact on H binding and on the resulting HER activity.<sup>57</sup> At high CO coverages, the H\* is actually weakened substantially during true operating conditions, an effect that suppresses the HER activity of Zn-Cu more so than with Zn (Figure S16). As revealed by the binding configurations, the two metals of the Zn-Cu site synergistically contribute to the COOH\* stabilization through Cu-C and Zn-O coordination, respectively (Figure 4C). CO and OH adsorption energies on individual Zn and Cu sites demonstrate the relatively stronger carbophilicity of Cu and stronger oxophilicity of Zn (Figure S17). Similarly, the Zn-Cu dual site in Zn<sub>1</sub>Cu<sub>8</sub> also has a more negative  $\Delta G_{ads}^{COOH*}$  than the monometallic Cu site (Figures 4D and S18). This is in agreement with the experimental results (Figure S12): an enhanced CO formation activity is observed on the Cu-rich Zn-Cu surface, while retaining the Cu-like ability for further reduction of CO into multicarbon products. The  $\Delta G_{ads}^{COOH*}$  as a function of the Zn/Cu composition displays a non-monotonic correlation (Figure 4D) and thus demonstrates the key role of the bimetallic sites in optimizing the reaction energetics.  $\Delta G_{ads}^{COOH*}$  and  $\Delta G_{ads}^{H*}$  are usually used to assess the CO<sub>2</sub>R to CO and HER activity, respectively,<sup>58</sup> and narrowing the difference between the two ( $\Delta(\Delta G) = \Delta G_{ads}^{COOH*} - \Delta G_{ads}^{H*}$ ) can lead to an onset potential of CO<sub>2</sub>R closer to that of HER. Note that the Volmer step in HER is inherently different in reaction nature from COOH formation and, thus,  $\Delta(\Delta G)$  can serve only as a relative measurement of CO<sub>2</sub>R to CO versus HER selectivity. Deeper understanding of the factors that control selectivity necessitates sophisticated electrochemical barrier calculations. Field stabilization of a bent CO<sub>2</sub>\* intermediate involved in COOH formation also contributes to favoring CO<sub>2</sub>R over the HER.<sup>59</sup> By comparing  $\Delta G_{ads}^{COOH*}$  and  $\Delta G_{ads}^{H*}$  in a range of stepped metal surfaces, we find that Zn-rich Zn<sub>11</sub>Cu<sub>1</sub> exhibits the smallest  $\Delta(\Delta G)$  among all the weak-binding elementary metals known for catalyzing CO<sub>2</sub>R to CO, whereas strong-binding metals with even smaller  $\Delta(\Delta G)$  suffer from a strong CO poisoning effect that limits their CO<sub>2</sub>R activity (Figure S19). CO poisoning is known to have a more profound effect on CO<sub>2</sub>R than HER, owing to the stronger lateral interaction between adsorbed CO\* and CO<sub>2</sub>R intermediates (CO\* and COOH\*) compared with H\*.<sup>60</sup> Overall, the reduced  $\Delta(\Delta G)$  from pristine Zn to Zn<sub>11</sub>Cu<sub>1</sub>, along with a moderate CO-binding strength on Zn<sub>11</sub>Cu<sub>1</sub>, comprises the main mechanistic insight for the enhanced CO production activity and selectivity on bimetallic Zn-Cu (5 s).

### Evaluating the long-term stability of Zn-Cu (5 s) and its performance in comparison to precious-metal catalysts

As shown by SEM and XPS data, the nanostructure and surface composition of the Zn-Cu (5 s) electrode are relatively unchanged after 1 h of CO<sub>2</sub>R testing (Figure S20). Longer-term testing over 20 h indicates that the CO production rate remains relatively stable; there is a minor decrease in selectivity for CO<sub>2</sub>R to CO (95%–86% FE) due to an increase in the HER over time (Figure S21). This increase in the HER is likely due to electroplating of trace impurities (e.g., transition metals) onto the cathode over long periods. Nonetheless, this initial stability test indicates that Zn-Cu (5 s) is promising for long-term application in CO<sub>2</sub>R electrolyzers.

As we discussed above, to the best of our knowledge there has not been a previous report of an earth-abundant bimetallic system that has better or similar intrinsic activity for CO<sub>2</sub>R to CO relative to Ag or Au, which are precious metals that are typically

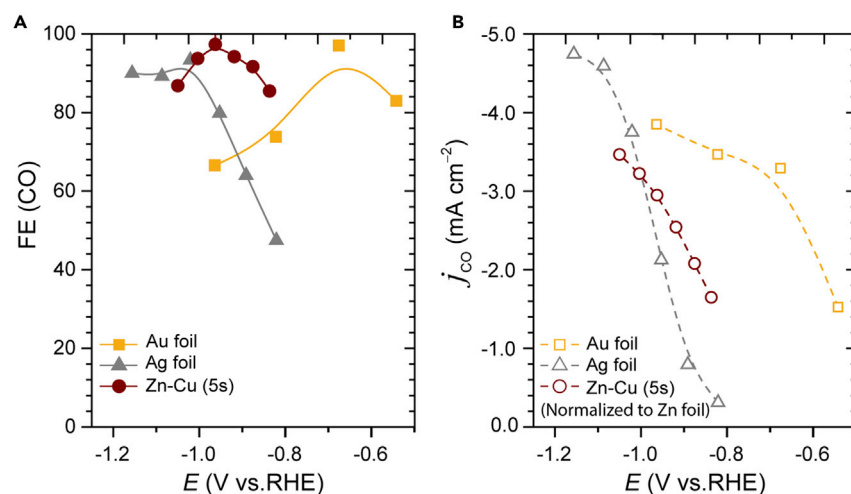


**Figure 5. CO<sub>2</sub>R performance comparisons among samples**

CO<sub>2</sub>R on galvanic-prepared Zn-Cu (5 s) and planar Ag and Au electrodes was assessed under the same conditions.<sup>10</sup> (A) Within a large potential window, the foil-based Zn-Cu (5 s) electrode showed higher selectivity for CO formation compared with foil-based Ag catalyst. (B) Zn-Cu (5 s) exhibits slightly higher CO partial-current density (normalized to Zn foil by ECSA) compared with Ag foil.

the major or only constituent of state-of-the-art catalysts. An analysis of CO<sub>2</sub>R on Zn-Cu (5 s), Ag, and Au foils as a function of the electrode potential demonstrated that Zn-Cu (5 s) has selectivity for CO production that is comparable to that of Ag and Au (Figure 5) and slightly improved intrinsic activity compared with Ag for CO<sub>2</sub>R to CO. As COOH formation usually involves the formation of a partially charged intermediate, bent CO<sub>2</sub><sup>\*</sup>, Au has an exceptional ability to stabilize this intermediate through strong interfacial electric fields, as it has the most positive potential of zero charge among metal catalysts (Figure S22).<sup>59</sup> While Zn-Cu (5 s) is less intrinsically active for CO<sub>2</sub>R to CO than Au, these results indicate that earth-abundant bimetallics could potentially serve as suitable replacements for precious-metal catalysts in CO<sub>2</sub> electrolyzers.

### CO<sub>2</sub>R to CO on Zn-Cu (powder) at high reaction rates

Based on the above insights, we integrated Zn-Cu catalysts onto GDEs to evaluate their performance within a GDE reactor at industrially relevant reaction rates. Commercial Zn powder was used to prepare Zn-Cu (powder) by utilizing the same galvanic-exchange procedure described above, and the particles were subsequently integrated onto GDEs to evaluate for CO<sub>2</sub>R in 1.0 M KOH (more details on the reaction conditions can be found in the experimental procedures). A direct comparison of Zn-Cu (powder) GDEs with Zn GDEs at a given current density shows significantly enhanced CO<sub>2</sub>R selectivity to CO and decreased HER selectivity for the Zn-Cu system (Figure 6 and Table S5), commensurate with the trends described above for the planar Zn-Cu and Zn electrodes. Notably, the differences in product selectivity are more pronounced at higher current densities, demonstrating the advantages of incorporating a small amount of Cu into Zn for applications that require high total reaction rates. Although our Zn-Cu GDEs are not as performant as state-of-the-art Ag-based GDEs,<sup>61,62</sup> we suggest that further research to optimize the catalyst layer<sup>61</sup> will close this performance gap. A considerable portion of the FE is unaccounted for in the measured product distribution for the GDEs with pure Zn, indicating possible corrosion or deposition processes that take place concurrent with CO<sub>2</sub>R. As Pourbaix analysis suggests that Zn is unlikely to be stable<sup>63</sup> under the

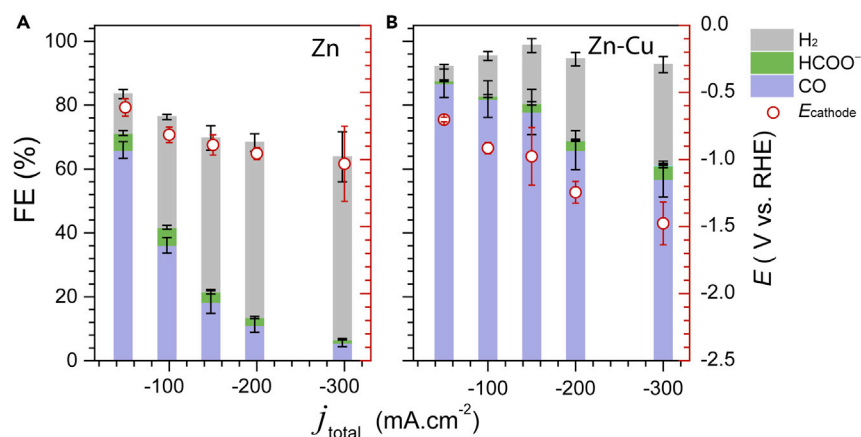


**Figure 6.**  $\text{CO}_2\text{R}$  in a gas-diffusion electrode reactor

Comparison of the electrocatalytic CO production of Zn (A) and Zn-Cu (powder) (B) gas-diffusion electrodes for  $\text{CO}_2\text{R}$ , at different current densities. Electrolysis was carried out in 1.0 M KOH, circulated at  $10\text{ mL min}^{-1}$ , with  $\text{CO}_2$  flow at 75 sccm. All data points are averaged from three individual measurements, the error bars represent the standard deviations (see Table S5).

alkaline conditions of our  $\text{CO}_2\text{R}$  measurements, we hypothesize that surface redox processes underpinning durability, such as corrosion and deposition, lead to losses in FE under these operating conditions. In contrast, nearly all the FE is accounted for with the Zn-Cu (powder) GDEs, suggesting that incorporating Cu imparts stability to Zn electrocatalysts. Future *operando* studies using synchrotron X-ray techniques could probe this dynamic reaction environment, providing insights into how to develop more robust systems under these harsh reaction conditions.

## Conclusion

We present bimetallic Zn-rich Zn-Cu as a highly efficient  $\text{CO}_2\text{R}$  to CO electrocatalyst prepared by a facile galvanic procedure. The Zn-Cu catalyst exhibits dramatically improved selectivity and activity for CO formation compared with pristine Zn and Cu electrocatalysts and, remarkably, also shows higher intrinsic activity than a planar Ag catalyst within the operating potential window from  $-0.8$  to  $-1.0$  V versus RHE. This enhanced intrinsic activity for CO formation on Zn-Cu catalysts is attributed to the electronic effect originating from the Cu adatoms on the Zn surface. DFT calculations suggest that the incorporation of Cu onto the Zn surface lowers the reaction energy (from 0.44 to 0.15 eV) of the PDS to form  $\text{COOH}^*$ , which improves CO production rates, while suppressing the HER due to a higher coverage of CO that impedes H adsorption. The changes in these relative energies rationalize the enhanced CO production activity and selectivity of Zn catalysts with Cu modification. Based on our fundamental studies involving planar electrodes, we then prepared a Zn-Cu powder catalyst and integrated it into a vapor-fed reactor. These GDEs also showed efficient  $\text{CO}_2$ -to-CO performance at industrially relevant reaction rates, consistent with expectations based on the prior studies. Overall, our work highlights the benefits of rationally designed bimetallic catalyst systems; a constructive ligand effect can modify the electronic properties of the bimetallic surfaces to tune the overall catalytic performance.

## EXPERIMENTAL PROCEDURES

### Resource availability

#### Lead contact

Further information and requests for resources and reagents should be directed to and will be fulfilled by the lead contact, Dr. Christopher Hahn ([hahn31@llnl.gov](mailto:hahn31@llnl.gov)).

#### Materials availability

This study did not generate new unique reagents. All the chemical materials and experimental procedures are summarized in the following.

#### Data and code availability

All data can be found in the supplemental information, which is available free of charge.

#### Chemical materials

Zinc foil (99.999%, 0.1 mm thick) was purchased from Alfa Aesar; zinc powder was purchased from Millipore Sigma (particle size 1–5  $\mu\text{m}$ , >99.8%); potassium hydroxide (semiconductor grade, 99.99% metal basis) was purchased from Sigma Aldrich; copper sulfate (99.99%) and hydrochloric acid (35% in water) were purchased from Fisher Scientific; and carbon dioxide (99.999%) was purchased from Air Gas. All chemical materials were used without further purification. All electrolyte solutions were prepared by deionized water from the Thermo Scientific Barnstead Nanopure water purification system (18.2 M $\Omega$  cm resistivity).

#### Preparation of the Zn-Cu electrodes: planar electrode

Zn foils were first mechanically polished by 600 grid and 1500 sandpaper and then rinsed with hydrochloric acid and water. The Zn foils were then immersed into a deaerated solution of  $\text{CuSO}_4$  (10 mM) at room temperature for a period of time (1–60 s) in order to galvanically exchange the Zn surface with Cu. The resulting foil was then carefully rinsed with water and dried with a  $\text{N}_2$  gun. The silver color of the Zn foil changed to dark gray after the galvanic treatment.

#### Thin-film-based electrode

The Cu-Zn thin-film electrodes were deposited by radio frequency magnetron co-sputtering of Cu and Zn metal targets onto 100 mm-diameter Si wafers with an approximately 170 nm  $\text{SiO}_2$  diffusion barrier and 10 nm Ti adhesion layer in a sputter-deposition system (Kurt J. Lesker, PVD) with  $10^{-5}$  Pa base pressure. The working atmosphere was composed of 0.8 Pa Ar gas. The substrate holder was rotating at a speed of 5 rpm, and the deposition proceeded for 8 min with no intentional substrate heating. The powers applied on Cu and Zn sources were adjusted to ensure the desired Cu-Zn composition, which was further confirmed by X-ray fluorescence (XRF) measurements using an EDAX Orbis Micro-XRF system. The composition gradient film was deposited similarly but without substrate rotation, such that the sputter-deposition gradient from each source resulted in a composition library thin film.

#### Gas-diffusion electrode

One gram of Zn powder was added to 10 mL of  $\text{CuSO}_4$  (10 mM) solution for 5 s, followed by quick filtration and rinsing with excess water. The resulting Zn-Cu powder was dried in air. It was then mechanically ground using a small laboratory mortar for 1 min until a fine and homogeneous powder was obtained. The powder was then suspended as a 10 mg mL $^{-1}$  aqueous ethanol ink supplemented with a perfluorinated sulfonic acid ionomer, Nafion, as a catalyst binder. The Nafion:catalyst ratio was set to 8.7 wt %. The ink was then sonicated for 10 min to ensure homogeneous dispersion of the catalyst and ionomer in the ink. One hundred thirty microliters of the as-prepared ink was then drop-casted onto 1 cm $^2$  gas-diffusion layers to reach a catalyst loading of 1.3 mg catalyst cm $^{-2}$ . During the deposition, the gas-diffusion layers were maintained on a 60°C hot plate to facilitate solvent evaporation. The

generated GDEs, so-called Zn-Cu (powder) GDEs, were then immediately tested for their electrochemical performance.

### Electrochemical measurements

A multichannel potentiostat (BioLogic VMP3) was used for all the electrochemical measurements in this study. A two-compartment electrochemical cell,<sup>36</sup> comprising a typical three-electrode system, was used for all the aqueous CO<sub>2</sub>R experiments: Zn-based electrodes as working electrodes (5.9 cm<sup>2</sup> geometric area exposed), a platinum foil as the counter electrode, and an Ag/AgCl electrode (Accumet) as the reference electrode. Selemion AMV (AGC, Inc.) was introduced as the anion-exchange membrane in between the counter and the working electrode compartments. A small distance (<0.5 cm) between the reference and the working electrodes was ensured for the electrolyte resistance. Dry CO<sub>2</sub> gas was humidified by KHCO<sub>3</sub> solution before flowing through the electrochemical cell, with a flow rate of 20 sccm regulated by a mass flow controller ( $\pi$ MFC, MKS Instruments). A 0.1 M solution of KHCO<sub>3</sub> saturated with CO<sub>2</sub> (pH 7.2) was prepared as the electrolyte.

The electrochemical performance of the Zn-Cu GDEs was assessed in a polycarbonate three-compartment cell additionally comprising (1) a Ni foil as the anode and (2) a leakless Ag/AgCl reference electrode (eDAQ). In each experiment, the Zn-Cu GDE was used as the working electrode with a 1.0 cm<sup>2</sup> geometric area exposed, on one side, to the catholyte and, on the other side, to a stream of gaseous CO<sub>2</sub>. KOH aqueous solutions (1 M) were employed as both the catholyte and the anolyte and were circulated at 10 mL min<sup>-1</sup> in the 6 mL cathodic and anodic compartments, using two auxiliary 25 mL reservoirs. A bipolar membrane (Fumasep FAS-50, FuelCell-Store) was used between the two compartments. The CO<sub>2</sub> flow rate was regulated using the mass flow controller and was set to 75 sccm.

### CO<sub>2</sub>R product analysis

The CO<sub>2</sub>R products (CO, hydrogen, and formate) were identified and quantified by using the same methods in our previous study.<sup>36</sup> To quantify the concentrations of CO and hydrogen, exhaust gas (1.0 mL) was sent to the gas chromatograph (SRI 8610C) from the working electrode compartment of the cell at different times during the electrolysis. The liquid product formate was quantified by using <sup>1</sup>H NMR spectroscopy (600 MHz, Varian Inova). All the experiments were repeated three times to establish statistical significance for the obtained data (Tables S1 and S5).

### High-throughput catalyst screening

Measurement of five Zn-Cu catalyst compositions (and pure Cu for comparison) was performed in a custom recirculating flow cell described previously.<sup>64</sup> Briefly, a 6 mm diameter thin film from the composition library, over which the composition was constant to within approximately 2–4 at %, was isolated using an O-ring-sealed three-electrode cell with bipolar membrane (Fumasep). Each 15 min electrolysis experiment was performed in batch reactor mode where recirculation of the electrolyte resulted in rapid concentration of reaction products for analytical quantification. Note that the surface concentration of dissolved CO<sub>2</sub> may be slightly lower than in traditional experiments, and the catalyst is continually exposed to reaction products from prior passes of the electrolyte.

### Physical characterization

The SEM images of the Zn-Cu electrodes were obtained using an FEI XL30 field emission scanning electron microscope. Non-contact atomic force microscopy



images were obtained by a Park Systems XE-70 or XE-100 scanning probe microscope equipped with a premounted Park Systems NSC15/Al BS tip and calculated topographical information (i.e., surface roughness) using Gwyddion software. The XPS spectra were collected by an SSI SProbe XPS spectrometer, using an incident Al K $\alpha$  radiation of 1,486 eV. The XRD patterns for the Zn-Cu electrodes were obtained using a PANalytical X'Pert diffractometer with an incident Cu K $\alpha$  radiation of 1.54056 Å.

XAS was performed in fluorescence mode with a Canberra 100 pixel Ge solid-state monolith detector at Beamline 11-2 at the Stanford Synchrotron Radiation Light-source. Both the Cu K-edge and the Zn K-edge results were calibrated to a foil reference measured simultaneously with the Zn-Cu bimetallic electrode. XAS results were processed in SixPACK (Sam Webb, SSRL) and the Athena module of the Demeter software package.<sup>65</sup> The lack of a prominent XANES feature at ~9,669 eV on the Zn K-edge, which has been attributed to the existence of a Zn-Cu alloy, could be due to the high Zn content of the alloy, which has been shown to reduce the intensity of this feature. The change in the Zn K-edge spectra edge energy between Zn-foil and Zn-Cu alloys was reported as ~1 eV in prior literature,<sup>54</sup> which is larger than the 0.3 eV observed in these measurements. This can be explained by the limited thickness of the alloy layer (~50–100 nm by XPS) relative to the thickness of the Zn foil substrate resulting in a measured intermediate edge shift between a Zn foil and a pure Zn-Cu material.

XRD characterization of the Zn-Cu composition library was performed using a Bruker DISCOVER D8 diffractometer with Cu K $\alpha$  radiation from a Bruker I $\mu$ S source. The X-ray spot size was limited to a 2 mm length scale, over which the composition was constant to within approximately 1–2 at %.

### Computational details

To simulate the above synthesized Zn-rich and Cu-rich Zn-Cu bimetallic catalysts, two stepped Zn-Cu surfaces, *hcp* Zn<sub>11</sub>Cu<sub>1</sub>(100) and face-centered cubic (*fcc*) Zn<sub>1</sub>Cu<sub>8</sub>(211), were constructed from the original *hcp* Zn(100) and *fcc* Cu(211) surfaces, respectively, by replacing a certain fraction of the step atoms with other metal atoms (Figure S14). Step atoms were selected for replacement due to their low cohesive energies, and the Zn:Cu ratio was set to be close to the experimental values. Pure *fcc* metal (211) surfaces and *hcp* Zn(100) surfaces were also simulated for comparison. Adsorption energies were calculated using DFT with a periodic plane-wave implementation and ultrasoft pseudopotentials using the QUANTUM ESPRESSO code,<sup>66</sup> interfaced with the Atomic Simulation Environment.<sup>67</sup> We applied the BEEF-vdW functional, which provides a reasonable description of van der Waals forces while maintaining an accurate prediction of chemisorption energies.<sup>68</sup> Plane-wave and density cutoffs were 500 and 5,000 eV, respectively, with a Fermi-level smearing width of 0.1 eV. In general, the adsorption energies on *fcc* (211) surfaces were evaluated using four-metal-layer (3 × 1) supercells with the bottom two metal layers constrained and a vacuum layer of 20 Å, and (4 × 4 × 1) Monkhorst-Pack k-point grids were used;<sup>69</sup> while for *hcp* (100) surfaces, four-metal-layer (3 × 2) supercells with the bottom two metal layers constrained and a vacuum layer of 20 Å, and (4 × 3 × 1) Monkhorst-Pack k-point grids were used. For the density of states calculation, (8 × 8 × 1) and (8 × 6 × 1) Monkhorst-Pack k-point grids<sup>69</sup> were used for the *fcc* (211) and *hcp* (100) surfaces, respectively. All structures were optimized until the force components were less than 0.05 eV Å<sup>-1</sup>. A dipole correction was applied to decouple the electrostatic interaction between the periodically

repeated slabs. The free energy of H<sub>2</sub>(g) was corrected by +0.09 eV as reported by Studt et al.<sup>70</sup> The free energy of CO<sub>2</sub>(g) was corrected by +0.33 eV to address the overestimation of CO<sub>2</sub> adsorption energies in DFT. Based on previous analysis,<sup>71,72</sup> the solvation energetic corrections of −0.25 and −0.06 eV were considered for COOH\* and CO\*, respectively.

The adsorption energies present in Figures 4, S16, and S18 are defined as:

$$\Delta G_{\text{ads}}^{\text{COOH}^*} = \mu(\text{slab} + \text{COOH}^*) - \mu(\text{slab}) - \mu(\text{CO}_2) - \frac{1}{2}\mu(\text{H}_2), \quad (\text{Equation 1})$$

$$\Delta G_{\text{ads}}^{\text{CO}^*} = \mu(\text{slab} + \text{CO}^*) + \mu(\text{H}_2\text{O}) - \mu(\text{slab}) - \mu(\text{CO}_2) - \mu(\text{H}_2), \quad (\text{Equation 2})$$

$$\Delta G_{\text{ads}}^{\text{H}^*} = \mu(\text{slab} + \text{H}^*) - \mu(\text{slab}) - \frac{1}{2}\mu(\text{H}_2). \quad (\text{Equation 3})$$

The free energy corrections to each species are shown in Table S4. The CO and OH adsorption energies present in Figure S17 were obtained on Cu(211) and Zn(100) and defined as:

$$\Delta E_{\text{ads}}^{\text{CO}^*} = E(\text{slab} + \text{CO}^*) - E(\text{slab}) - E(\text{CO}), \quad (\text{Equation 4})$$

$$\Delta E_{\text{ads}}^{\text{OH}^*} = E(\text{slab} + \text{OH}^*) + \frac{1}{2}E(\text{H}_2) - E(\text{slab}) - E(\text{H}_2\text{O}). \quad (\text{Equation 5})$$

All energies of relaxed structures are listed in the supplemental information and hosted online as well at the Catalysis-Hub repository<sup>73</sup> at <https://www.catalysis-hub.org/publications/WangSyneristic2020>.

## SUPPLEMENTAL INFORMATION

Supplemental information can be found online at <https://doi.org/10.1016/j.checat.2021.05.006>.

## ACKNOWLEDGMENTS

The galvanic-exchange synthesis, physical and electrochemical characterization, and DFT calculations on Zn-Cu bimetallics are based on work performed by the Joint Center for Artificial Photosynthesis, a DOE Energy Innovation Hub, supported through the Office of Science of the U.S. Department of Energy under Award DE-SC0004993. Combinatorial high-throughput measurements of sputtered Cu-Zn catalysts are based on work performed by the Liquid Sunlight Alliance, which is supported by the U.S. Department of Energy, Office of Science, Office of Basic Energy Sciences, Fuels from Sunlight Hub under Award DE-SC0021266. Part of this work was performed at the Stanford Nano Shared Facilities (SNSF), supported by the National Science Foundation under Award ECCS-1542152. Use of the Stanford Synchrotron Radiation Lightsource, SLAC National Accelerator Laboratory, is supported by the U.S. Department of Energy, Office of Science, Office of Basic Energy Sciences under Contract DE-AC02-76SF00515. Additional thanks go to the Stanford NMR Facility. L.W. thanks the Knut and Alice Wallenberg Foundation for financial support and the National University of Singapore and Ministry of Education – Singapore for its financial support through Tier-1 projects with grants R-279-000-622-133 and R-279-000-622-731.

## AUTHOR CONTRIBUTIONS

Conceptualization, L.W., T.F.J., and C.H.; methodology, L.W., H.P., S.L., Z.Q., D.K., M.B.S., J.A.Z.Z., D.W., L.K., L.Z., and Y.L.; investigation, L.W., H.P., S.L., Z.Q., D.K.,

M.B.S., J.A.Z.Z., D.W., L.K., L.Z., Y.L., and M.F.; writing – original draft, L.W., H.P., and S.L.; writing – review & editing, L.W., H.P., S.L., Z.Q., D.K., M.B.S., J.A.Z.Z., D.W., L.K., L.Z., Y.L., M.F., J.G., F.A.-P., T.F.J., and C.H.; funding acquisition, J.G., F.A.-P., T.F.J., and C.H.; supervision, J.G., F.A.-P., T.F.J., and C.H.

## DECLARATION OF INTERESTS

The authors declare no competing interests.

Received: January 26, 2021

Revised: April 18, 2021

Accepted: May 6, 2021

Published: June 7, 2021

## REFERENCES

- Rostrup-Nielsen, J.R., Sehested, J., and Nørskov, J.K. (2002). Hydrogen and synthesis gas by steam- and CO<sub>2</sub> reforming. *Adv. Catal.* 47, 65–139.
- Luk, H.T., Mondelli, C., Ferré, D.C., Stewart, J.A., and Pérez-Ramírez, J. (2017). Status and prospects in higher alcohols synthesis from syngas. *Chem. Soc. Rev.* 46, 1358–1426.
- Haas, T., Krause, R., Weber, R., Demler, M., and Schmid, G. (2018). Technical photosynthesis involving CO<sub>2</sub> electrolysis and fermentation. *Nat. Catal.* 1, 32–39.
- Energy Technology Systems Analysis Programme. (2010). Syngas Prod. From Coal. <http://large.stanford.edu/courses/2013/ph241/kall>.
- Peter, S.C. (2018). Reduction of CO<sub>2</sub> to chemicals and fuels: a solution to global warming and energy crisis. *ACS Energy Lett.* 3, 1557–1561.
- Davis, S.J., Lewis, N.S., Shaner, M., Aggarwal, S., Arent, D., Azevedo, I.L., Benson, S.M., Bradley, T., Brouwer, J., Chiang, Y., et al. (2018). Net-zero emissions energy systems. *Science* 360, 1419.
- Jouny, M., Luc, W., and Jiao, F. (2018). General techno-economic analysis of CO<sub>2</sub> electrolysis systems. *Ind. Eng. Chem. Res.* 57, 2165–2177.
- Chen, Y., Li, C.W., and Kanan, M.W. (2012). Aqueous CO<sub>2</sub> reduction at very low overpotential on oxide-derived Au nanoparticles. *J. Am. Chem. Soc.* 134, 19969–19972.
- Liu, M., Pang, Y., Zhang, B., De Luna, P., Voznyy, O., Xu, J., Zheng, X., Dinh, C.T., Fan, F., Cao, C., et al. (2016). Enhanced electrocatalytic CO<sub>2</sub> reduction via field-induced reagent concentration. *Nature* 537, 382–386.
- Yoon, Y., Hall, A.S., and Surendranath, Y. (2016). Tuning of silver catalyst mesostructure promotes selective carbon dioxide conversion into fuels. *Angew. Chem. Int. Ed.* 55, 15282–15286.
- Ma, M., Trzeźniowski, B.J., Xie, J., and Smith, W.A. (2016). Selective and efficient reduction of carbon dioxide to carbon monoxide on oxide-derived nanostructured silver electrocatalysts. *Angew. Chem. Int. Ed.* 55, 9748–9752.
- Zhu, W., Michalsky, R., Metin, Ö., Lv, H., Guo, S., Wright, C.J., Sun, X., Peterson, A.A., and Sun, S. (2013). Monodisperse Au nanoparticles for selective electrocatalytic reduction of CO<sub>2</sub> to CO. *J. Am. Chem. Soc.* 135, 16833–16836.
- Lu, Q., Rosen, J., Zhou, Y., Hutchings, G.S., Kimmel, Y.C., Chen, J.G., and Jiao, F. (2014). A selective and efficient electrocatalyst for carbon dioxide reduction. *Nat. Commun.* 5, 1–6.
- Wang, Y., Cao, L., Libretto, N.J., Li, X., Li, C., Wan, Y., He, C., Lee, J., Gregg, J., Zong, H., et al. (2019). Ensemble effect in bimetallic electrocatalysts for CO<sub>2</sub> reduction. *J. Am. Chem. Soc.* 141, 16635–16642.
- He, J., Dettelbach, K.E., Huang, A., and Berlinguette, C.P. (2017). Brass and bronze as effective CO<sub>2</sub> reduction electrocatalysts. *Angew. Chem. Int. Ed.* 56, 16579–16582.
- Rasul, S., Anjum, D.H., Jedidi, A., Minenkov, Y., Cavallo, L., and Takanabe, K. (2015). A highly selective copper-indium bimetallic electrocatalyst for the electrochemical reduction of aqueous CO<sub>2</sub> to CO. *Angew. Chem. Int. Ed.* 54, 2146–2150.
- Yin, Z., Gao, D., Yao, S., Zhao, B., Cai, F., Lin, L., Tang, P., Zhai, P., Wang, G., Ma, D., et al. (2016). Highly selective palladium-copper bimetallic electrocatalysts for the electrochemical reduction of CO<sub>2</sub> to CO. *Nano Energy* 27, 35–43.
- Sun, K., Cheng, T., Wu, L., Hu, Y., Zhou, J., MacLennan, A., Jiang, Z., Gao, Y., Goddard, W.A., and Wang, Z. (2017). Ultrahigh mass activity for carbon dioxide reduction enabled by gold-iron core-shell nanoparticles. *J. Am. Chem. Soc.* 139, 15608–15611.
- Lamaison, S., Blanchard, J., Giaume, D., Fontecave, M., Lamaison, S., Wakerley, D., Blanchard, J., and Montero, D. (2020). High-current-density CO<sub>2</sub> to-CO electroreduction on Ag-alloyed Zn dendrites at elevated pressure. *Joule* 4, 395–406.
- Sarraz, S., Garcia-Esparza, A.T., Jedidi, A., Cavallo, L., and Takanabe, K. (2016). Cu-Sn bimetallic catalyst for selective aqueous electroreduction of CO<sub>2</sub> to CO. *ACS Catal.* 6, 2842–2851.
- Kim, D., Resasco, J., Yu, Y., Asiri, A.M., and Yang, P. (2014). Synergistic geometric and electronic effects for electrochemical reduction of carbon dioxide using gold-copper bimetallic nanoparticles. *Nat. Commun.* 5, ncomms5948.
- Lamaison, S., Wakerley, D., Montero, D., Taverna, D., Giaume, D., Mercier, D., Blanchard, J., and Tran, N. (2019). Zn – Cu alloy nanofoams as efficient catalysts for the reduction of CO<sub>2</sub> to syngas mixtures with a potential-independent H<sub>2</sub>/CO ratio. *ChemSusChem*, 511–517.
- Hori, Y., Murata, A., and Ito, S. (1990). Enhanced evolution of CO and suppressed formation of hydrocarbons in electroreduction of CO<sub>2</sub> at a copper electrode modified with cadmium. *Chem. Lett.* 1231–1234.
- Li, Q., Fu, J., Zhu, W., Chen, Z., Shen, B., Wu, L., and Xi, Z. (2017). Tuning Sn-Catalysis for electrochemical reduction of CO<sub>2</sub> to CO via the core/shell Cu/SnO<sub>2</sub> structure. *ACS Catal.* 8, 4290–4293.
- Hu, X.M., Hval, H.H., Bjerglund, E.T., Dalgaard, K.J., Madsen, M.R., Pohl, M.M., Welter, E., Lamagni, P., Buhl, K.B., Bremholm, M., et al. (2018). Selective CO<sub>2</sub> reduction to CO in water using earth-abundant metal and nitrogen-doped carbon electrocatalysts. *ACS Catal.* 8, 6255–6264.
- Jiang, K., Siahrostami, S., Zheng, T., Hu, Y., Hwang, S., Stavitski, E., Peng, Y., Dynes, J., Gangisetty, M., Su, D., et al. (2018). Isolated Ni single atoms in graphene nanosheets for high-performance CO<sub>2</sub> reduction. *Energy Environ. Sci.* 11, 8–14.
- Li, X., Bi, W., Chen, M., Sun, Y., Ju, H., Yan, W., Zhu, J., Wu, X., Chu, W., Wu, C., et al. (2017). Exclusive Ni – N 4 sites realize near-unity CO selectivity for electrochemical CO<sub>2</sub> reduction. *J. Am. Chem. Soc.* 139, 14889–14892.
- Koshy, D.M., Chen, S., Lee, D.U., Stevens, M.B., Abdellah, A.M., Dull, S.M., Chen, G., Nordlund, D., Gallo, A., Hahn, C., et al. (2020). Understanding the origin of highly selective CO<sub>2</sub> electroreduction to CO on Ni, N-doped carbon catalysts. *forschungsartikel. Angew. Chem. Int. Ed.* 132, 4072–4079.
- Pan, Y., Lin, R., Chen, Y., Liu, S., Zhu, W., Cao, X., Chen, W., Wu, K., Cheong, W., Wang, Y., et al. (2018). Design of single-atom Co – N<sub>5</sub> catalytic site: a robust electrocatalyst for CO<sub>2</sub> reduction with nearly 100% CO selectivity and

- remarkable stability. *J. Am. Chem. Soc.* **148**, 4218–4221.
30. Yang, H.B., Hung, S.F., Liu, S., Yuan, K., Miao, S., Zhang, L., Huang, X., Wang, H.Y., Cai, W., Chen, R., et al. (2018). Atomically dispersed Ni(ii) as the active site for electrochemical CO<sub>2</sub> reduction. *Nat. Energy* **3**, 140–147.
31. Huan, T.N., Ranjbar, N., Rouse, G., Sougrati, M., Zitolo, A., Mougél, V., Jaouen, F., and Fontecave, M. (2017). Electrochemical reduction of CO<sub>2</sub> catalyzed by Fe-N-C materials: a structure-selectivity study. *ACS Catal* **7**, 1520–1525.
32. Ren, S., Joulé, D., Salvatore, D., Torbensen, K., Wang, M., Robert, M., and Berlinguette, C.P. (2019). Molecular electrocatalysts can mediate fast, selective CO<sub>2</sub> reduction in a flow cell. *Science* **365**, 367–369.
33. Lin, S., Diercks, C.S., Zhang, Y., Kornienko, N., Yaghi, O.M., and Chang, C.J. (2015). Covalent organic frameworks comprising cobalt porphyrins for catalytic CO<sub>2</sub> reduction in water. *Science* **349**, 1208–1212.
34. Zhang, X., Wu, Z., Zhang, X., Li, L., Li, Y., Xu, H., Li, X., and Yu, X. (2017). Highly selective and active CO<sub>2</sub> reduction electrocatalysts based on cobalt phthalocyanine/carbon nanotube hybrid structures. *Nat. Commun.* **8**, 14675, ncomms14675.
35. Zhanaidarova, A., Jones, S.C., Despagne-Ayoub, E., Pimentel, B.R., and Kubiak, C.P. (2019). Re(tBu-bpy)(CO)<sub>3</sub> Cl supported on multi-walled carbon nanotubes selectively reduces CO<sub>2</sub> in water. *J. Am. Chem. Soc.* **141**, 17270–17277.
36. Wang, L., Nitopi, S.A., Wong, A.B., Snider, J.L., Nielander, A.C., Morales-guio, C.G., Orazov, M., Higgins, D.C., Hahn, C., and Thomas, F. (2019). Electrochemically converting carbon monoxide to liquid fuels by directing selectivity with electrode surface area. *Nat. Catal.* **2**, 702–708.
37. Talanquer, V., Oxtoby, D., Islam, M.F., Zhang, J., Collings, P.J., Yodh, A.G., Gleiter, H., Perepezko, J., Terrones, M., Dwyer, J.R., et al. (2012). Molecular Fe catalyst. *Science* **338**, 90–94.
38. Kaminsky, C.J., Wright, J., and Surendranath, Y. (2019). Graphite-conjugation enhances porphyrin electrocatalysis. *ACS Catal.* **9**, 3667–3671.
39. Noda, H., Ikeda, S., Oda, Y., Imai, K., Maeda, M., Ito, K., Ideka, S., Oda, Y., Imai, K., Maeda, M., et al. (1990). Electrochemical reduction of carbon dioxide at various metal electrodes in aqueous potassium hydrogen carbonate solution. *Bull. Chem. Soc. Jpn.* **63**, 2459–2462.
40. Kuhl, K.P., Hatsukade, T., Cave, E.R., Abram, D.N., Kibsgaard, J., and Jaramillo, T.F. (2014). Electrocatalytic conversion of carbon dioxide to methane and methanol on transition metal surfaces. *J. Am. Chem. Soc.* **136**, 14107–14113.
41. Hori, Y. (2008). Electrochemical CO<sub>2</sub> reduction on metal electrodes. *Mod. Asp. Electrochem.* **89**–189.
42. Peterson, A., and Nørskov, J. (2012). Activity descriptors for CO<sub>2</sub> electroreduction to methane on transition-metal catalysts. *J. Phys. Chem. Lett.* **3**, 251–258.
43. Ren, D., Ang, B.S.H., and Yeo, B.S. (2016). Tuning the selectivity of carbon dioxide electroreduction toward ethanol on oxide-derived CuZn catalysts. *ACS Catal.* **6**, 8239–8247.
44. Abe, H., and Miyauchi, M. (2017). Selective electro- or photo-reduction of carbon dioxide to formic acid using a Cu–Zn alloy catalyst. *J. Mater. Chem. A* **5**, 12113–12119.
45. Feng, Y., Li, Z., Liu, H., Dong, C., Wang, J., Kulinich, S.A., and Du, X. (2018). Laser-prepared CuZn alloy catalyst for selective electrochemical reduction of CO<sub>2</sub> to ethylene. *Langmuir* **34**, 13544–13549.
46. Ren, D., Gao, J., Pan, L., Wang, Z., Luo, J., Zakeeruddin, S.M., Hagfeldt, A., and Grätzel, M. (2019). Atomic layer deposition of ZnO on CuO enables selective and efficient electroreduction of carbon dioxide to liquid fuels. *Angew. Chem. Int. Ed.* **58**, 15036–15040.
47. Wichern, C.M., De Cooman, B.C., and Van Tyne, C.J. (2004). Surface roughness changes on a hot-dipped galvanized sheet steel during deformation at low strain levels. *Acta Mater.* **52**, 1211–1222.
48. Bard, A.J., and Faulkner, L.R. (2001). *Electrochemical Methods: Fundamentals and Applications* (Wiley), p. c1980.
49. Zuo, J., and Erbe, A. (2010). Optical and electronic properties of native zinc oxide films on polycrystalline Zn. *Phys. Chem. Chem. Phys.* **12**, 11467–11476.
50. Sankar, R., Navaneethan, M., Mani, G.K., Ponnusamy, S., Tsuchiya, K., Muthamizhchelvan, C., Kawasaki, S., and Hayakawa, Y. (2016). Influence of Al doping on the structural, morphological, optical, and gas sensing properties of ZnO nanorods in fl uence of Al doping on the structural, morphological, optical, and gas sensing properties of ZnO nanorods. *J. Alloys Compd.* **698**, 555–564.
51. Timoshenko, J., Jeon, H.S., Sinev, I., Haase, F.T., Herzog, A., and Roldan Cuenya, B. (2020). Linking the evolution of catalytic properties and structural changes in copper-zinc nanocatalysts using operando EXAFS and neural-networks. *Chem. Sci.* **11**, 3727–3736.
52. Luo, W., Zhang, Q., Zhang, J., Moiolli, E., Zhao, K., and Züttel, A. (2020). Electrochemical reconstruction of ZnO for selective reduction of CO<sub>2</sub> to CO. *Appl. Catal. B Environ.* **273**, 119060.
53. Espinós, J.P., Morales, J., Barranco, A., Caballero, A., Holgado, J.P., and González-Elipé, A.R. (2002). Interface effects for Cu, CuO, and Cu<sub>2</sub>O deposited on SiO<sub>2</sub> and ZrO<sub>2</sub>. XPS determination of the valence state of copper in Cu/SiO<sub>2</sub> and Cu/ZrO<sub>2</sub> catalysts. *J. Phys. Chem. B* **106**, 6921–6929.
54. Yeh, H.C., and Azároff, L.V. (1967). X-ray K absorption edges of alloys. III. Copper-zinc and nickel-zinc systems. *J. Appl. Phys.* **38**, 4034–4038.
55. Hall, A.S., Yoon, Y., Wuttig, A., and Surendranath, Y. (2015). Mesostucture-Induced selectivity in CO<sub>2</sub> reduction Catalysis. *J. Am. Chem. Soc.* **137**, 14834–14837.
56. Mezzavilla, S., Horch, S., Stephens, I.E.L., Seger, B., and Chorkendorff, I. (2019). Structure sensitivity in the electrocatalytic reduction of CO<sub>2</sub> with gold catalysts. *Angew. Chem. Int. Ed.* **58**, 3774–3778.
57. Cave, E.R., Shi, C., Kuhl, K.P., Hatsukade, T., Abram, D.N., Hahn, C., Chan, K., and Jaramillo, T.F. (2018). Trends in the catalytic activity of hydrogen evolution during CO<sub>2</sub> electroreduction on transition metals. *ACS Catal.* **8**, 3035–3040.
58. Landers, A.T., Fields, M., Torelli, D.A., Xiao, J., Hellstern, T.R., Francis, S.A., Tsai, C., Kibsgaard, J., Lewis, N.S., Chan, K., et al. (2018). The predominance of hydrogen evolution on transition metal sulfides and phosphides under CO<sub>2</sub> reduction conditions: an experimental and theoretical study. *ACS Energy Lett.* **3**, 1450–1457.
59. Ringe, S., Morales-Guio, C.G., Chen, L.D., Fields, M., Jaramillo, T.F., Hahn, C., and Chan, K. (2020). Double layer charging driven carbon dioxide adsorption limits the rate of electrochemical carbon dioxide reduction on Gold. *Nat. Commun.* **11**, <https://doi.org/10.1038/s41467-019-13777-z>.
60. Liu, X., Xiao, J., Peng, H., Hong, X., Chan, K., and Nørskov, J.K. (2017). Understanding trends in electrochemical carbon dioxide reduction rates. *Nat. Commun.* **8**, ncomms15438.
61. Mahyoub, S.A., Qaraah, F.A., Chen, C., Zhang, F., Yan, S., and Cheng, Z. (2020). An overview on the recent developments of Ag-based electrodes in the electrochemical reduction of CO<sub>2</sub> to CO. *Sustain. Energy Fuels* **4**, 50–67.
62. Wang, R., Haspel, H., Pustovarenko, A., Dikhtiarenko, A., Russikh, A., Shterk, G., Osadchii, D., Ould-Chikh, S., Ma, M., Smith, W.A., et al. (2019). Maximizing Ag utilization in high-rate CO<sub>2</sub> electrochemical reduction with a coordination polymer-mediated gas diffusion electrode. *ACS Energy Lett.* **4**, 2024–2031.
63. Beverskog, B., and Puigdomenech, I. (1997). Revised pourbaix diagrams for zinc at 25–300°C. *Corros. Sci.* **39**, 107–114.
64. Jones, R.J.R., Wang, Y., Lai, Y., Shinde, A., and Gregoire, J.M. (2018). Reactor design and integration with product detection to accelerate screening of electrocatalysts for carbon dioxide reduction. *Rev. Sci. Instrum.* **89**, 124102.
65. Ravel, B., and Newville, M. (2005). Athena, ARTEMIS, HEPHAESTUS: data analysis for X-ray absorption spectroscopy using IFEFFIT. *J. Synchrotron Radiat.* **12**, 537–541.
66. Giannozzi, P., Baroni, S., Bonini, N., Calandra, M., Car, R., Cavazzoni, C., Chiarotti, G.L., Cococcioni, M., Dabo, I., Corso, A.D., et al. (2009). Quantum ESPRESSO: a modular and open-source software project for quantum simulations of materials. *J. Phys. Condens. Matter* **21**, 395502.
67. Bahn, S.R., and Jacobsen, K.W. (2002). An object-oriented scripting interface to a legacy electronic structure code. *Comput. Sci. Eng.* **4**, 56–66.
68. Wellendorff, J., Lundgaard, K.T., Møgelhøj, A., Petzold, V., Landis, D.D., Nørskov, J.K., Bligaard, T., and Jacobsen, K.W. (2012). Density functionals for surface science:

- exchange-correlation model development with Bayesian error estimation. *Phys. Rev. B* **85**, 235149.
69. Monkhorst, H.J., and Pack, J.D. (1976). Special points for Brillouin-zone integrations. *Phys. Rev. B* **13**, 5188–5192.
  70. Studt, F., Behrens, M., Kunkes, E.L., Thomas, N., Zander, S., Tarasov, A., Schumann, J., Frei, E., Varley, J.B., Abild-Pedersen, F., et al. (2015). The mechanism of CO and CO<sub>2</sub> hydrogenation to methanol over Cu-based catalysts. *ChemCatChem* **7**, 1105–1111.
  71. Peterson, A.A., Abild-Pedersen, F., Studt, F., Rossmeisl, J., and Nørskov, J.K. (2010). How copper catalyzes the electroreduction of carbon dioxide into hydrocarbon fuels. *Energy Environ. Sci.* **3**, 1311–1315.
  72. Ludwig, T., Gauthier, J.A., Brown, K.S., Ringe, S., Nørskov, J.K., and Chan, K. (2019). Solvent–adsorbate interactions and adsorbate-specific solvent structure in carbon dioxide reduction on a stepped Cu surface. *J. Phys. Chem. C* **123**, 5999–6009.
  73. Winther, K.T., Hoffmann, M.J., Boes, J.R., Mamun, O., Bajdich, M., and Bligaard, T. (2019). Catalysis-Hub.org, an open electronic structure database for surface reactions. *Sci. Data* **6**, 75.